JOURNAL OF GEOPHYSICAL RESEARCH, VOL. 118, 1-15, doi:10.1029/2012JC008221, 2013

Estimation of the sunglint radiance field from optical satellite imagery over open ocean: multidirectional approach and polarization aspects

Tristan Harmel,[1,2] and Malik Chami[1,2,3]

Received 18 May 2012; revised 31 October 2012; accepted 3 November 2012.

[1] Radiometric satellite measurements over the ocean are greatly affected by the contribution of the direct sunlight reflected on the ruffled ocean (so-called sunglint). Sunglint produces radiance that can far exceed the radiance scattered by both the atmosphere and ocean layers. Knowledge of the sunglint radiance is required in many remote sensing applications using radiance and polarization information (e.g., retrieval of aerosol or hydrosol optical properties, sensor calibration). The Cox and Munk model is currently used for estimating sunglint signal, but its accuracy is mainly limited by the mandatory use of wind speed data sets. An algorithm (so-called polarization-based atmospheric correction glint) was developed based on the original multidirectional and polarization radiometric measurements of the Polarization and Anisotropy of Reflectances for Atmospheric Sciences Coupled with Observations from a Lidar satellite mission. The method enables to accurately estimate the radiance and the polarization terms of the sunglint signal. The strength of the algorithm is to quantify the sunglint radiation using the Polarization and Anisotropy of Reflectances for Atmospheric Sciences Coupled with Observations from a Lidar data without any a priori information on the actual sea state A relevant application of the algorithm is proposed to better detect the pixels influenced by clouds provided that ancillary data of wind speed are used.

Citation: Harmel, T., and M. Chami (2013), Estimation of the sunglint radiance field from optical satellite imagery over open ocean: multidirectional approach and polarization aspects, *J. Geophys. Res.*, *118,* doi:10.1029/2012JC008221.

1. Introduction

[2] The sparkling patch of sunlight reflected on the ocean can be readily seen in any optical images acquired from the shore or the deck of a ship as well as from a plane or a satellite platform. The peak of intensity due to the sunlight reflection on the rough sea surface, commonly referred to as sunglint, occurs in the vicinity of the theoretical location of the specular reflection spot that would be obtained for a flat sea. The whole area where sunglint is present is called Sun glitter and its extent is spread by a myriad of glints generated by reflection of sunlight on the facets of the water surface that are tilted toward the observer [*Torrance et al*., 1966]. *Hulburt* [1934] worked out the geometry of Sun glitter as it relates to Sun elevation and wave slope, but did not consider the detailed optics of single glints. Later investigations conducted by *Cox and Munk* [1954a, 1954b] led to quantitative and statistical results about the link between sunglint and sea state. Their results have been widely used in many topics of remote sensing. The contribution of the sunglint signal to the top of atmosphere radiance is much higher than that of the radiance scattered by both the atmosphere and the ocean layers. Hence, it is of great interest to determine how the sunglint influences the satellite radiometric measurements [*Gordon*, 1978].

[3] The performances of the inversion algorithms of the satellite measurements to retrieve aerosol parameters or ocean color radiometry are generally strongly impacted by the sunglint contamination of pixels. Therefore, the sunglint radiance component needs to be accurately estimated either to be explicitly exploited by inversion algorithms to derive some geophysical products or to filter the contaminated data within satellite images. In most cases, the sunglint contaminated pixels are masked and excluded from data analysis. Note, however, that *Wang and Bailey* [2001] proposed some low threshold values of the sunglint radiance component for which the sunglint contribution to the total signal could be removed thus allowing the application of inversion algorithms of the sunglint free radiance. The great majority of remote sensing inversion algorithms relies on the *Cox and Munk* (CM) model [*Cox and Munk*, 1954a, 1954b], which uses the wind speed and wind direction as inputs, to determine the sunglint radiance component. However, the CM

[1]Université Pierre et Marie Curie, Laboratoire Océanographie de Villefranche, 06230Villefranche sur Mer, France.
[2]CNRS, Laboratoire Océanographie de Villefranche Villefranche sur Mer, France.
[3]Institut Universitaire de France.

Corresponding author: T. Harmel, Université Pierre et Marie Curie, Laboratoire Océanographie de Villefranche, 06230 Villefranche sur Mer, France. (harmel@obs-vlfr.fr)

©2012. American Geophysical Union. All Rights Reserved.
2169-9275/13/2012JC008221

model can suffer either from a lack of accuracy of the input wind parameters or from a deviation of the slope statistics relatively to the real-world sea state conditions [*Kay et al*., 2009]. Since the pioneering work of *Cox and Munk* [1954a, 1954b], a great number of studies has been dedicated to gaining understanding of light interaction with the ruffled sea surface. As examples, the importance of investigating the interaction of light with a rough ocean was clearly showed through the recent interdisciplinary observational and modeling efforts of the RaDyO program [*Dickey et al*., 2011], through the development of new instrumentation aiming at characterizing the effects of sea surface on light [*Darecki et al*., 2011; *Ottaviani et al*., 2008b], and through radiative transfer modeling accounting for a rough ocean [*Ottaviani et al*., 2008a; *You et al*., 2011].

[4] Sunglint information obtained in the visible and near-infrared wavelengths can be a useful source of data for many applications. For example, the sunglint spectral information can be used to cross-calibrate different satellite spectral bands [*Hagolle et al*., 2004; *Nicolas et al*., 2006] or for polarization measurement calibration [*Toubbe et al*., 1999]. Sunglint measurements can also provide information about the atmosphere such as water vapor content [*Aoki et al*., 2002; *Gao and Kaufman*, 2003; *Kleidman et al*., 2000] or the absorbing component of aerosols [*Kaufman et al*., 2002]. In addition, sunglint features can be used, as in the original study of *Cox and Munk* [1954a, 1954b, 1956], to derive the state of the sea surface [*Breon and Henriot*, 2006; *Ebuchi and Kizu*, 2002; *Ross and Dion*, 2007] or even the surface wind speeds [*Breon and Henriot*, 2006; *Harmel and Chami*, 2012]. They could also reveal internal waves within the ocean [*Jackson*, 2007]. The sunglint properties have been recently exploited for oil spill monitoring [*Chust and Sagarminaga*, 2007; *Hu et al*., 2009]. Corrections of satellite data for the sunglint signal could also be of great interest to increase the accuracy of retrieval of below-surface conditions and oceanic biomass [*Hu*, 2010; Steinmetz *et al*., 2011]. Thus, if the sunglint radiance and polarization components can be accurately estimated, it could lead to important applications.

[5] The Polarization and Anisotropy of Reflectances for Atmospheric Sciences Coupled with Observations from a Lidar (PARASOL) satellite sensor was orbiting among the five Sun-synchronous satellites forming the so-called A-Train until the end of 2009. Since then, the French space agency Centre National d'Etudes Spatiales (CNES) decided to drift its orbit for maintenance purposes. The originality of PARASOL sensor mostly relies on its capability to measure the polarization state of light (namely the Stokes parameters I, Q, and U) for various wavelengths and for a high number of directions (up to 16 directions) [*Parol et al*., 2004]. An atmospheric correction algorithm, the so-called multidirectionality and POLarization-based Atmospheric Correction (POLAC) was recently developed to exploit the original features of the PARASOL sensor (i.e., multidirectionality and polarization) for improving retrieval of aerosol optical properties and ocean color radiometry [*Harmel and Chami*, 2011]. In the present study, the multidirectionality and polarization properties of PARASOL sensor are analyzed in depth for determining the contribution of sunglint component to the top of atmosphere signal. The underlying idea is to use the multidirectionality and polarization signatures of the radiation, rather than the sole monodirectional radiance signal as it is currently used for usual ocean color sensors (e.g., SeaWiFS, Moderate Resolution Imaging Spectroradiometer (MODIS) or Medium-Resolution Imaging Spectrometer (MERIS) sensors), as robust physical constraints to quantify the sunglint signal. In this objective, a new method (so-called POLAC-glint) is developed and implemented within the POLAC algorithm to identify the sunglint pattern in the PARASOL satellite images.

[6] The paper is organized in five sections as follows. Theoretical background of the sunlight reflection on ruffled sea surface is first described. Then, the main features of the PARASOL satellite sensor and the inversion scheme of the published POLAC algorithm are summarized (section 2). The new method developed to detect the sunglint signal (POLAC-glint algorithm) is presented in section 3. In section 4, the POLAC-glint algorithm is applied to actual PARASOL images and an original extension of POLAC-glint approach for the detection of cloud edge is proposed. The validation of the sunglint components (Stokes parameters) retrieved by POLAC-glint algorithm is presented in section 5.

2. Data and Method

2.1. Sun Glint Signal at the Top of the Atmosphere

[7] The normalized radiance at the top of the atmosphere (denoted by I_{TOA}) is defined as follows:

$$I_{\mathrm{TOA}} = \frac{\pi I_{\mathrm{mes}}}{F_0} \tag{1}$$

where F_0 is the extraterrestrial solar irradiance and I_{mes} is the upward radiance measured at the satellite level for a given geometry defined by the solar zenith angle, θ_{s}, the viewing zenith angle, θ_{v}, and the relative azimuth between the Sun and the satellite sensor, ϕ. The definition of equation 1 can be extended to the Stokes vector $\mathbf{S} = [I,Q,U,V]^{\mathrm{T}}$ for a given target (i.e., a given bidirectional reflectance distribution function). Note that the superscript T stands for the transpose of the vector. The Stokes vector describes electromagnetic radiation in terms of measurable quantities, including polarization state of electromagnetic field. In this study, the Stokes vector is defined with respect to the meridian plane, which is the plane determined by the viewing direction of the satellite and the local zenith. Note that the V component of the Stokes vector is commonly assumed negligible with respect to the other components (I, Q, and U) at the top of atmosphere [*Coulson*, 1988; *Kattawar et al*., 1976]. Thus, the V component will not be further discussed in the current study.

[8] For incoherent light, the property of additivity of Stokes vector components enables us to decompose the TOA signal at a given wavelength, which could be expressed in normalized radiance unit as follows [*Gordon and Brown*, 1974; *Gordon and Wang*, 1994; *Tanre et al*., 1979; *Vermote et al*., 1997]:

$$\begin{aligned}\mathbf{S_{TOA}} = T_g(\theta_s,\theta_v)\Big[&\mathbf{S_{atm}} + T_{\mathrm{down}}(\theta_s)T_{\mathrm{up}}(\theta_v)\mathbf{S_g} \\ &+ t_{\mathrm{down}}(\theta_s)t_{\mathrm{up}}(\theta_v)\left(\mathbf{S_{wc}} + \mathbf{S_w^+}\right)\Big]\end{aligned} \tag{2}$$

where T_{g} is the transmittance due to the absorption of atmospheric gases, T_{down} and T_{up} are the downward and

the upward direct transmittances, respectively, as well as t_{down} and t_{up} are the downward and the upward total transmittances, respectively. Note that only the direct transmittance T_{up} is used as the weighting factor of $\mathbf{S_g}$ (and not t_{up}) because the sunglint contribution is defined in this study as being composed of the sole direct light radiation (i.e., no scattered light). It should be highlighted that such a definition is frequently adopted in the literature (see for example [*Zhang and Wang*, 2010]). $\mathbf{S_{TOA}}$, $\mathbf{S_{atm}}$, $\mathbf{S_g}$, $\mathbf{S_{wc}}$, and $\mathbf{S_w^+}$ hold for the Stokes vectors of the TOA, atmosphere, sunglint, foam, and water-leaving components, respectively. The term $\mathbf{S_{wc}}$ can be calculated based on the foam cover, which is parameterized with the wind speed and with the spectral reflectance of foam [*Frouin et al*., 1996; *Koepke*, 1984; *Monahan*, 1971]. Because the foam is composed of a very high volumetric concentration of small bubbles, which induce a large amount of multiple scattering events in the whitecap layer [*Kokhanovsky*, 2004a, 2004b], the polarized signal of the whitecaps component should be small. Thus, the polarization terms Q_{wc} and U_{wc} could be neglected. The term $\mathbf{S_w^+}$ corresponds to the fraction of light exiting the ocean layer (i.e., just above the sea surface). The terms $\mathbf{S_{atm}}$ and $\mathbf{S_w^+}$ are computed through radiative transfer computations based on the OSOA (Ordres successifs Océan-Atmosphére) model [*Chami et al*., 2001]. It should be reminded that the OSOA model does not consider the agitated sea surface (flat sea). The gaseous transmittance T_g is calculated using the model "6SV" [*Kotchenova et al*., 2006; *Vermote et al*., 1997] coupled with the total ozone mapping spectrometer data set.

[9] The Stokes vector that corresponds to the sunglint signal at the top of the atmosphere, namely $\mathbf{S_g}$, can be easily calculated for a flat surface according to the Fresnel's reflection matrix. If the ocean surface is roughened by the wind, a myriad of reflected images of the Sun will reach the satellite sensor due to specular reflection from various waves and wavelets of the sea surface. In the model developed by *Cox and Munk* [1954a, 1954b, 1956], the wave slope probability distribution of the facets of the given orientation is combined to the appropriate Fresnel's reflection matrix to compute the term $\mathbf{S_g}$ of equation 2. Note that, in this model, the probability distribution corresponds to a Gram-Charlier series decomposition, which was parameterized on wind speed and wind direction from airborne measurements [*Cox and Munk*, 1954a].

[10] Figure 1 shows the Stokes parameters I_g, Q_g, and U_g of the sunglint contribution to the TOA signal at 865 nm computed according to the Cox and Munk model for an aerosol optical thickness of 0.1 at 550 nm, a solar zenith

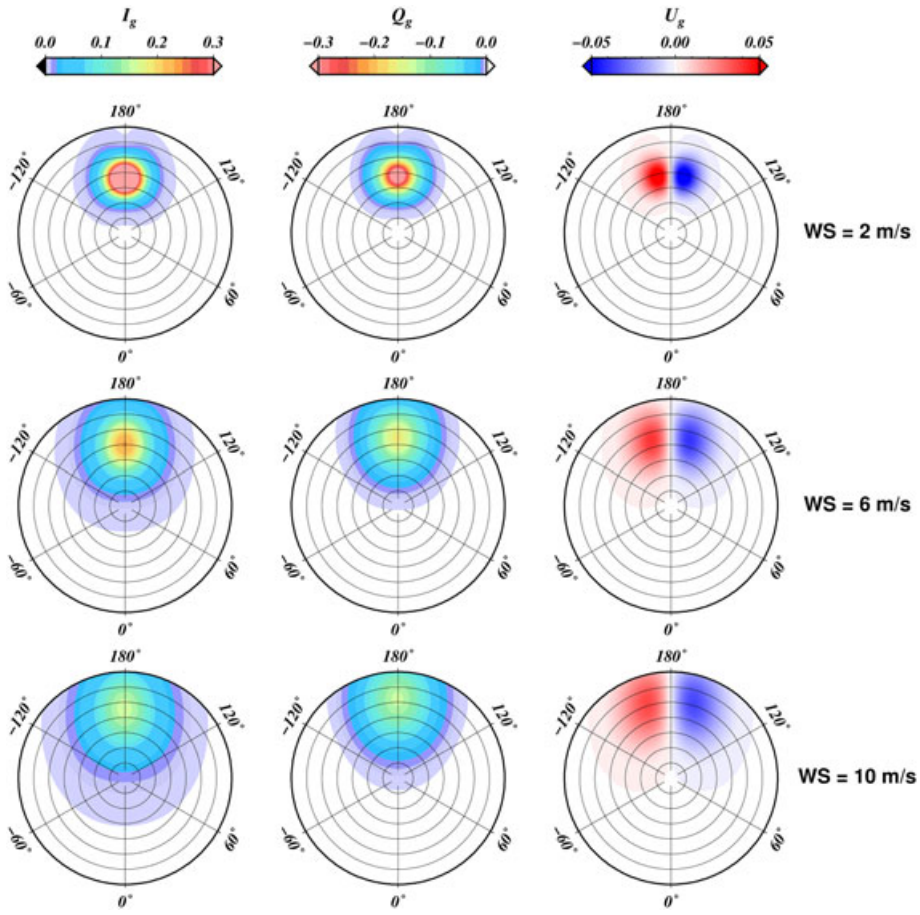

Figure 1. Stokes parameters of the sunglint contribution to the top-of-atmosphere signal, namely I_g, Q_g, and U_g (dimensionless), at 865 nm for an aerosol optical thickness of 0.1 at 550 nm, a solar zenith angle of 35°, a wind azimuth of 0° and wind speeds *ws* of 2, 6, and 10 m s^{-1}. In the polar diagrams, the concentric circles represent the viewing angles by step of 10° (from 0° to 70°). The solid lines represent the relative azimuth angle with respect to the Sun by step of 60°.

angle of 35° and several wind speed values. It can be readily observed in Figure 1 that the influence of the sunglint is restricted to a small range of directional configurations for each of the Stokes parameter at low wind speed values ($2\,m\,s^{-1}$). However, the range of directions affected by the sunglint enlarges with increasing wind speeds. Almost one third of the viewing directions could be affected by sunglint when the value of wind speed is $10\,m\,s^{-1}$. Over the studied wind speed range, from $2\,m\,s^{-1}$ to $10\,m^{-1}$, the values of the Stokes parameters attributed to the sunglint component of the TOA signal are generally one order of magnitude greater than those that are attributed to scattering process induced by both the atmosphere and ocean layers. It is interesting to highlight that some geometries are fairly never affected by sunglint whatever the wind speed. The use of the Cox and Munk model is thus relevant to identify these geometries since they do not exhibit a high sensitivity to wind speed conditions.

2.2. PARASOL Images

[11] The PARASOL satellite mission (French space agency CNES) was primarily dedicated to improving knowledge on the radiative and microphysical properties of clouds and aerosols by measuring the intensity and the polarization state of light in several different viewing directions. The onboard PARASOL sensor is the third generation of the POLDER (Polarization and Directionality of the Earth Reflectances) instrument [*Deschamps et al*., 1994; *Deuze et al*., 2001; *Herman et al*., 2005]. The optical device of PARASOL is characterized by a wide field of view (~114°). A CCD matrix array detector (242*274 elements) allows acquisition of two-dimensional images of the Earth [*Deschamps et al*., 1994] for a spatial resolution of about 6 km per 7 km at nadir viewing direction.

[12] One of the main features of interest of PARASOL is its ability to acquire successive images that partially overlap each other. Thus, a given ground target is observed at various viewing geometries (up to 16) along the satellite track. Therefore, a part of the bidirectional reflectance distribution function of both the atmosphere and ground target can be measured using PARASOL. The total acquisition time for a whole multidirectional sequence is performed within a 4 min time window for which the geophysical parameters of the scene can be assumed as virtually similar [*Deschamps et al*., 1994]. The Stokes parameter *I*, as defined in equation 1, is measured in nine spectral bands centered on wavelengths ranging from 443 to 1020 nm. Note that the use of the channel 443 nm is not recommended by CNES because it could be contaminated by instrumental stray light within the sensor itself [*Fougnie et al*., 2007]. Three spectral channels, namely 490, 670, and 865 nm, are equipped with polarizers thus allowing the measurement of the polarization Stokes parameters *Q* and U. Three successive polarization measurements are performed within a total time lapse of 0.6 s. The noise equivalent normalized radiance of PARASOL data is about 4.10^{-4} [*Fougnie et al*., 2007].

[13] Figure 2 shows an example of successive acquisitions of the PARASOL satellite (true-color images) along its orbit over the western Mediterranean Sea. The impact of the sunglint is noticeably variable from one acquisition to another in this example. Over a given area, the sunglint contribution to the TOA signal might be observed for certain acquisitions only (Figures 2d–2h) whereas its impact vanishes for other acquisitions, which corresponds to viewing geometries that are far from the specular reflection of the Sun on the sea surface (Figures 2a–2c). It is also worth noting that distinctive sunglint patterns are observed on those successive PARASOL images depending on the roughness of the sea surface. In Figure 2g, for instance, the zone centered on 43°N, 4°E appears dark in comparison to the bright surrounding areas southward. As will be discussed later (in section 4.1, Figure 6), such a dark area is not affected by sunglint from a geometry point of view while the brighter areas are. The qualitative observation of Figure 2 points out that an accurate quantification of the sunglint contribution to satellite signal requires an analysis on a pixel-by-pixel basis as will be investigated later in this paper.

2.3. Data Inversion Scheme

[14] An atmospheric correction algorithm, the so-called POLAC, was recently developed based on the multidirectional and polarization data of the PARASOL sensor [*Harmel and Chami*, 2011]. The POLAC algorithm was used to process the PARASOL data of this study. This section provides an overview of the general principles of the POLAC algorithm. The reader could refer to *Harmel and Chami* [2011] for details.

[15] The POLAC algorithm is composed of two principal phases, hereafter noted phase P1 and P2. The phase P1 deals with the retrieval of the aerosol optical thickness along with the respective proportion of fine and coarse aerosol modes. The water-leaving radiance retrieval is then carried out in P2 based on the P1's outputs. The two phases make use of an optimization scheme for retrieving the geophysical parameters of interest. The optimization process is achieved by minimizing a cost function, which is built from the difference between PARASOL measurements and simulations. The simulations are performed using the vector radiative transfer model OSOA [*Chami et al*., 2001]. Note that OSOA model was specifically designed for simulating the light field and the polarization state of light in a coupled atmosphere-ocean system.

[16] The water-leaving radiance can be assumed negligible in the near-infrared spectral bands (dark water) because of the high water absorption occurring in clear open oceans in this range of the spectrum [*Gordon and Clark*, 1981]. Thus, the top-of-atmosphere total radiance (i.e., Stokes parameter *I*) measured by a satellite sensor at those wavelengths is informative on the atmosphere layer only and can thus be used to estimate the aerosol optical properties [*Antoine and Morel*, 1999; *Fukushima et al*., 1998; *Gordon*, 1997; *Gordon and Wang*, 1994]. At 865 nm, the water leaving signal remains below 10^{-4} in reflectance unit, which is lower than the noise of the PARASOL sensor. Thus, the Stokes parameter *I* measured by PARASOL in the near-infrared part of the spectrum is not altered by the submarine light field. It could be used to detect various contributors to the TOA signal that are not linked to underwater applications such as the aerosols, the sunglint signal or the surface whitecaps.

[17] In the visible part of the spectrum, the water-leaving radiance cannot be neglected anymore (i.e., it might represent up to 20% of TOA radiance). It should be accounted for in the decomposition of the radiance measured by the

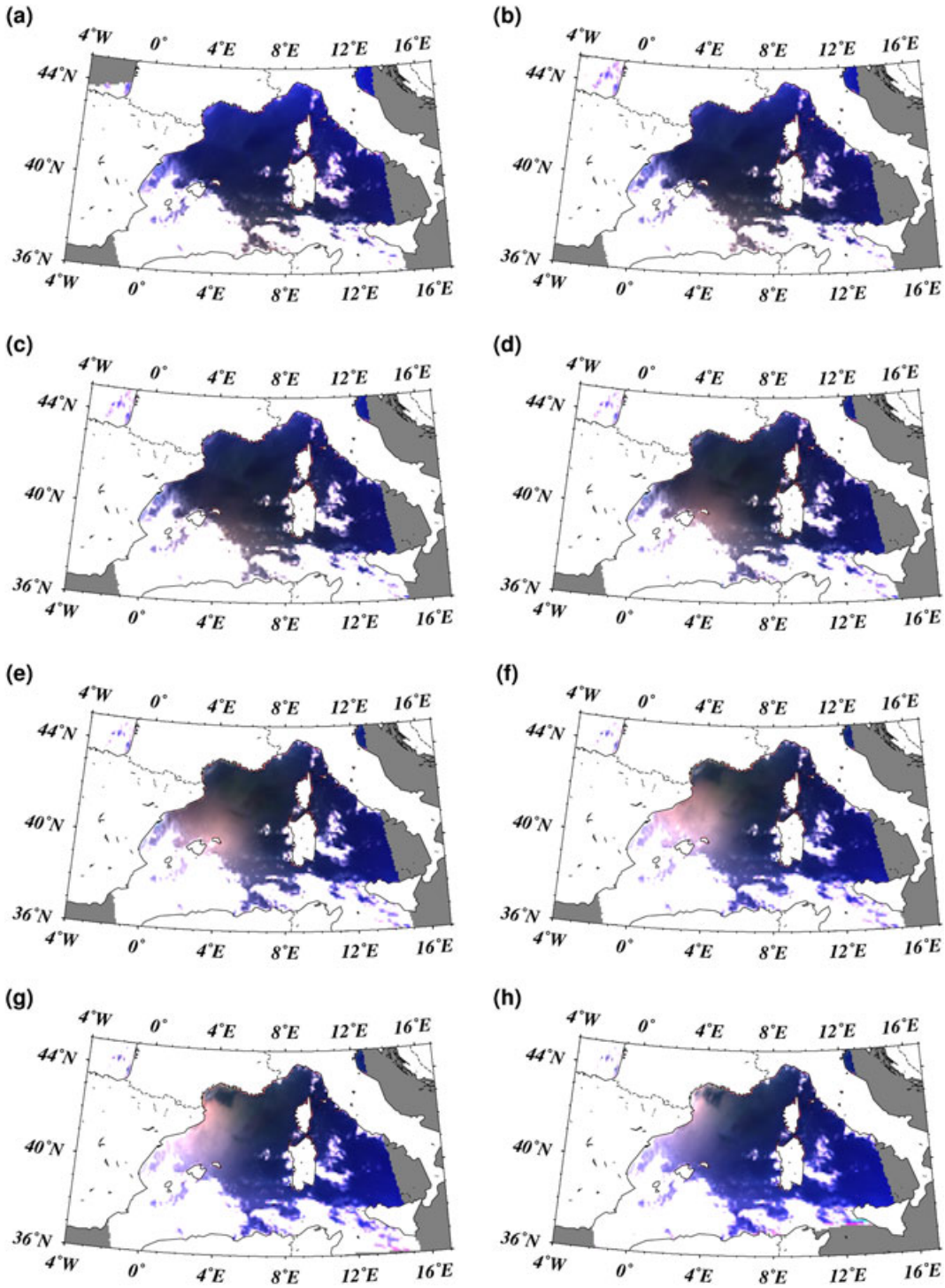

Figure 2. Successive acquisitions of the PARASOL satellite (true-color images) along its orbit over the western Mediterranean Sea on 5 May 2006. The impact of the sunglint on Figures 2d to 2h is visible on the western part of the image (bright area); the highly reflective clouds appear in white on the images.

satellite sensor (see equation 2). In contrast, the polarized signal measured by PARASOL in the blue-green part of the visible spectrum (like 490 nm) is fairly insensitive to the variations of the phytoplankton biomass concentration in open ocean waters [*Chami*, 2007; *Harmel and Chami*, 2008]. It should be noted that a recent study confirmed this finding for this part of the visible spectrum [*Chowdhary et al*., 2012]. Therefore, the polarization signal measured by PARASOL at 490, 670, and 865 nm is clearly exploitable for the retrieval of the aerosol optical properties regardless of the phytoplankton biomass concentration over open ocean.

[18] The phase P1 of POLAC algorithm fully exploits the invariance properties of the polarized visible signal with biomass concentration. The phase P1 is subdivided into two iterative steps. First, the aerosol optical thickness is determined based on the Stokes parameter I in the near-infrared

band, namely at 865 nm. Second, the Q and U parameters are used to estimate the best bimodal aerosol model, which is defined as a couple of a fine mode and a coarse mode. The respective proportion between the fine and coarse mode is retrieved as well. Note that optimal results are obtained when the inversion procedure is carried out considering simultaneously all the available directional measurements when dealing with the retrieval of the aerosol modes and direction by direction when dealing with the estimation of the optical thickness [see *Harmel and Chami*, 2011, Figure 2]. The optimization process is achieved by minimizing a cost function, which is built from the difference between PARASOL measurements and radiative transfer simulations. When the cost function does not decrease anymore after a given iteration, the procedure is stopped. The convergence of the procedure is typically obtained after two or three iterations. Based on the retrieved values of aerosol optical properties, the phase P2 is activated to derive the water-leaving radiance in the visible spectrum (i.e., PARASOL bands centered on 490, 565, 670 nm). The water leaving radiance is retrieved by matching the measurements of scalar TOA radiance (since the polarized radiance is not depending on the phytoplankton biomass as discussed above) with radiative transfer simulations computed for various hydrosol compositions of the oceanic layer. The overall procedure is carried out for all the available directional observations of a given PARASOL pixel. Note that a special attention is paid to the phase P1 in this paper since any sunglint contribution to the TOA signal needs to be first accurately identified to properly achieve the retrieval of aerosol optical properties and water-leaving radiance.

3. Sun Glint and Cloud Edge Detection

3.1. Estimation of the Sun Glint Stokes Vector: POLAC-glint Algorithm

[19] The inversion of satellite data using atmospheric correction algorithms such as POLAC algorithm is performed only if measurements are not contaminated by undesirable geophysical phenomena such as Sun reflection on the ocean surface or presence of clouds, in particular thin clouds or cloud edge. Therefore, it is of great interest to identify and filter out pixels of satellite images that are affected by such phenomena to avoid erroneous retrievals. The sunglint contamination of the multidirectional PARASOL measurements strongly depends on the viewing geometry as previously shown (Figures 1 and 2). For a given PARASOL ground target, only a limited number of viewing directions might be contaminated by sunglint [*Deuze et al*., 2000]. In this latter case, the presence of sunglint significantly increases the signal detected at top-of-atmosphere. Despite the fact that the sunglint radiance is spectrally nearly white, the increase of the sunglint signal at satellite level is more pronounced at 865 nm (which is the wavelength that is used for the retrieval of aerosol optical thickness τ_a in POLAC) because the atmospheric transmittance is higher than that at shorter wavelengths. Therefore, the application of the POLAC algorithm for viewing directions contaminated by sunglint would lead to a large overestimation of τ_a since the reflection of the sunglint signal onto the sea surface was ignored within POLAC algorithm when modeling the radiance at the top of atmosphere. In contrast, the retrieval of τ_a for the same PARASOL ground target observed in a direction that is not affected by sunglint would lead to more realistic values. It should be pointed out that the abundance of aerosols, which is quantified by the parameter τ_a, is not dependent on the viewing direction. As a result, given a ground target, the retrieved values of τ_a for each viewing direction will exhibit a great dispersion when some of the viewing directions are contaminated by sunglint (as it will be shown later in Figure 5).

[20] Based on this latter consideration, a specific sunglint filtering procedure was implemented within POLAC to identify and quantify the sunglint signal as measured by PARASOL data. In the phase *P1* of POLAC, the aerosol optical thickness $\tau_{a,dir}(i)$ is retrieved for each i^{th} single viewing direction using comparisons between measurements and radiative transfer simulations of the radiance I at 865 nm, as mentioned in section 3.2. The median value of the $\tau_{a,dir}(i)$ is the final output τ_a of the retrieval algorithm. Therefore, the dispersion of the retrieved τ_a can be estimated as follows [*Harmel and Chami*, 2011]:

$$\Delta\tau_a = \sqrt{\frac{\sum_{i=1}^{N_{dir}} \left(\tau_{a,dir}(i) - median\left(\tau_{a,dir}\right)\right)^2}{N_{dir} - 1}} \quad (3)$$

where N_{dir} is the total number of available viewing directions of the PARASOL pixel. Note that the aerosol optical depth is derived from the fit performed on the multidirectional simulations of the actual data, as described in *Harmel and Chami* [2011]. These simulations account for the variability of the phase matrix of the aerosol model retrieved by POLAC. Thus, it is important to highlight that the uncertainty in the phase matrix is already embedded within the procedure that retrieves the aerosol optical depth. Within the POLAC procedure that allows estimating τ_a, the value of $\Delta\tau_a$ is used to determine the directional consistency between the measured values of I(865 nm), which could be possibly affected by sunglint, and the POLAC simulated ones, which do not include any sunglint contribution. If certain directions are affected by sunglint, the directional consistency between measured and modeled values would vanish; as a result, $\Delta\tau_a$ would be much higher than $\Delta\tau_a$ that will be derived when dealing with a pixel for which none of the directions are affected by sunglint. Because the presence of sunglint tends to significantly overestimate τ_a, the filtering of the contaminated directions is performed within the inversion scheme of POLAC by iteratively removing directions leading to the highest value of the retrieved $\tau_{a,dir}$.

[21] Such an iterative procedure is summarized as follows: (i) POLAC is applied to the N_{dir} available directions of a PARASOL pixel; (ii) the value of $\Delta\tau_a$ is calculated; (iii) if $\Delta\tau_a$ is greater than a given threshold, the direction for which the retrieved value of $\tau_{a,dir}$ is the highest is removed; (iv) a new iteration of POLAC is performed on the N_{dir}-1 remaining directions. Note that if $\Delta\tau_a$ increases between two successive iterations, the procedure is stopped. Because the uncertainty on aerosol optical thickness obtained from satellite measurements was shown to be linearly dependent on τ_a [*Mishchenko et al*., 2007; *Tanre et al*., 1997], the threshold that is applied at step (iii) corresponds to a linear function of τ_a as well. This threshold was set to $0.03 + 0.05\tau_a$ following the type of threshold variation adopted by the MODIS

aerosol retrieval team [*Remer et al.*, 2005]. Note that an offset value of 0.03 was considered here to be more representative of the PARASOL sensor [*Breon et al.*, 2011]. Because the performance of the aerosol model retrieval by POLAC degrades when the number of available viewing directions is low, typically lower than three, the pixel is removed when less than three available directions remains at the end of the procedure. An overview of the overall procedure is shown in Figure 3.

[22] Then, the aerosol model, the aerosol optical thickness, and the water-leaving radiance are retrieved by the POLAC algorithm applied to the set of directions identified as outside of the glint influence. Based on these retrievals, the term $\mathbf{S_{atm}}$, $\mathbf{S_w^+}$ as well as the atmospheric transmittances can easily be calculated for all the directions (inside and outside the glint pattern) through radiative transfer computations whose results have been stored in look-up tables data files. The whitecaps component $\mathbf{S_{wc}}$ of equation 2 can be assumed negligible in comparison to the other terms for wind speeds up to 10 m s^{-1} [*Frouin et al.*, 1996]. Moreover, the polarization terms Q_{wc} and U_{wc} could be neglected due to the high number of multiple scattering events induced by whitecaps as discussed in section 2.1. Thus, the Stokes vector of the sunglint signal can be expressed by the following equation:

$$\mathbf{S_g} = \frac{1}{T_{down}(\theta_s)T_{up}(\theta_v)}\left[\frac{\mathbf{S_{TOA}}}{T_g(\theta_s,\theta_v)} - \mathbf{S_{atm}} - t_{down}(\theta_s)t_{up}(\theta_v)\mathbf{S_w^+}\right] \quad (4)$$

[23] As an illustration, the sunglint filter that has been implemented in POLAC algorithm (so-called POLAC-glint method) is now applied to PARASOL ground targets that are observed at various directions. Figure 4 shows the radiance at 865 nm measured by PARASOL over the Mediterranean sea (diamonds in Figure 4) and simulated using either POLAC algorithm (red circles) or the Cox and Munk model (black circles). Note that the Cox and Munk model is used here as first guess for computing the sunglint signal (the ECMWF (European Centre for Medium-Range Weather Forecasts) wind speed is used as input of CM model). One ground target has been selected specifically out of the sunglint spot along the PARASOL track (Figures 4a and 4b); another ground target was selected specifically to include viewing directions that are contaminated by sunglint (Figures 4c and 4d). When measurements are acquired off the sunglint (Figures 4a and 4b), simulations and satellite data are in good agreement for all the available directions in comparison with the case where the target is located within the sunglint

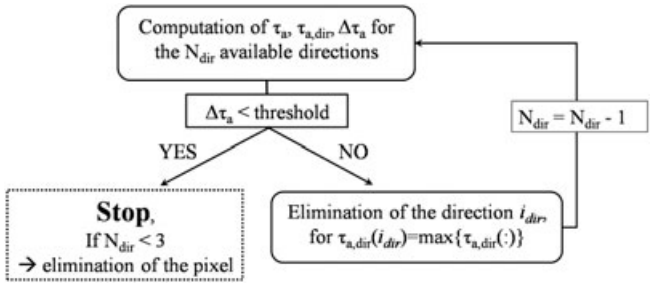

Figure 3. Flowchart diagram of the procedure used within POLAC-glint algorithm to detect directions affected by sunglint.

pattern (Figures 4c and 4d). It is interesting to observe here that all directions of CM simulations having non-null values of sunglint radiance as shown in Figures 4c and 4d are fairly well identified by POLAC-glint algorithm. The Figure 5 reports the values of the aerosol optical thickness for each direction of the pixel of the Figure 4c. It can be readily seen that the sunglint signal tends to artificially increase the retrieved value of the aerosol optical thickness (up to five times larger than the actual value) when the directions are contaminated by the sunglint (white dots). Conversely, the values that are retrieved outside the sunglint influence are virtually constant. Thus, the aerosol optical parameters are correctly retrieved as illustrated through the consistency between simulations (red circles, Figure 4c) and measurements at angles for which measurements are not contaminated by sunglint (e.g., angles lower than –30°, black diamonds, Figure 4c).

3.2. Identification of Cloud Influence

[24] Undetected thin clouds or vicinity of clouds could impact the satellite data by enhancing significantly the amplitude of the received signal. As a result, a number of viewing directions may be wrongly identified as contaminated by sunglint when using the POLAC-glint algorithm. Data that are affected by clouds cannot be properly used for aerosol observation or ocean color radiometry purposes. As a first approximation, it could be assumed that the effects of clouds are not consistent with the radiation field that emerges from a cloud-free atmosphere containing air molecules and aerosols only. The impact of these effects on PARASOL data thus differs depending on the directional acquisitions. To correctly identify pixels impacted by clouds, adjustments were added into the POLAC-glint procedure. On the basis of the procedure described in Figure 3, the identification of cloud influence consists of three steps: (i) the first iteration of the sunglint filter procedure is carried out; (ii) if a viewing direction is identified as contaminated by sunglint by the POLAC-glint algorithm, the sunglint radiance for the same viewing direction is estimated based on the Cox and Munk model for two values of wind speed equal to the ECMWF wind speed value plus or minus 1 m s^{-1}, (iii) if the two modeled sunglint radiances are smaller than the instrumental radiometric noise threshold of PARASOL, this means that the viewing direction is supposed to be totally out of the sunglint observation geometry. Note that the use of two wind speed values enables to limit the impact of the wind speed uncertainty, which has been evaluated close to 1 m s^{-1} [*Breon and Henriot*, 2006]. The corresponding viewing direction has thus been wrongly identified by the algorithm as contaminated by sunglint. Note that the ancillary wind speed data are uniquely used here to provide the theoretical geometry of pixels affected by sunglint; they are not used to derive the actual sunglint Stokes vector. The corresponding pixel is then qualified as "cloud influenced direction" outside of sunglint; (iv) finally, if more than three directions are identified as "cloud influenced direction", the iterative process stops and the whole PARASOL ground target is flagged as "cloud influenced" pixel. Such type of pixel is no longer considered in the POLAC atmospheric correction processing.

4. Pixel Classification

[25] The POLAC-glint algorithm was applied to several PARASOL images over open ocean areas. Prior to applying

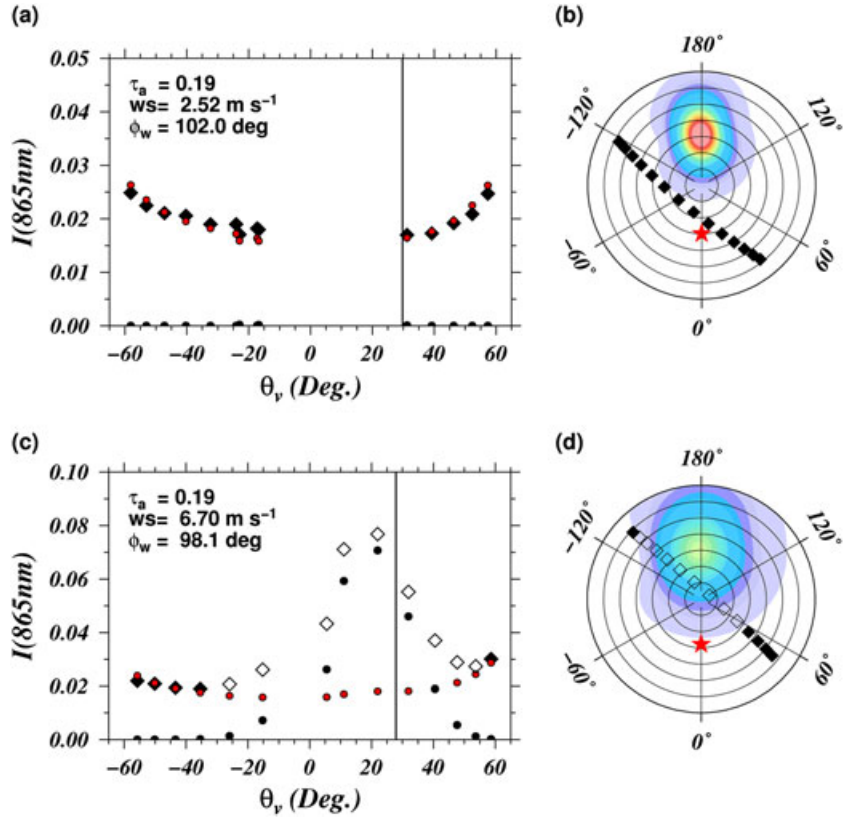

Figure 4. Examples of application of the POLAC-glint algorithm to PARASOL data acquired on 5 May 2006 over the Mediterranean sea. (a) Top of atmosphere radiance at 865 nm measured by PARASOL for a ground target that is not contaminated by sunglint (black diamonds) and radiance simulated by POLAC algorithm (red circles) and Cox and Munk model (black circle). (b) Polar diagram showing geometries of the multidirectional acquisition of PARASOL. Cox and Munk model computation of the sunglint is superimposed (colored pattern). (c) and (d) Similar to Figures 4a and 4b for a ground target that is contaminated by sunglint (white diamonds). The viewing angle is negative when the relative azimuth angle is between 90° and 270°. The Sun position is illustrated by a vertical line in Figures 4a and 4c and by a red star in Figures 4b and 4d. The color scale used is the same as the one used in Figure 1.

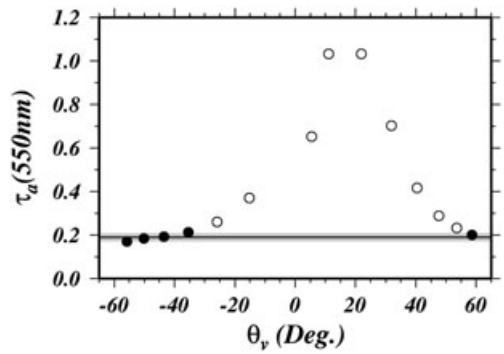

Figure 5. Illustration of the aerosol optical thicknesses retrieved for each direction of the PARASOL pixel of Figure 4c. The values retrieved at directions that are detected as contaminated by the sunglint are represented in white. The black line indicates the actual value retrieved by the POLAC algorithm (i.e., $\tau_a = 0.19$); the shaded area corresponds to plus or minus the estimated uncertainty.

POLAC-glint method, the pixels that are identified as totally cloudy by the operational data processing of PARASOL provided by CNES are eliminated. In this section, the performances of both POLAC-glint algorithm and POLAC cloud identification are discussed.

4.1. Sun Glint Pixels

[26] The standard sunglint identification procedure that is based on the Cox and Munk model [*Wang and Bailey*, 2001] was first applied to the PARASOL images. This standard procedure uses the wind speed and wind direction taken from the ECMWF data set. A given viewing direction is identified as contaminated by sunglint when the sunglint normalized radiance at the top of atmosphere simulated using Cox and Munk's model is greater than the noise equivalent normalized radiance of PARASOL.

[27] Figure 6a shows the number of viewing directions that should be affected by sunglint when applying the Cox and Munk model to a PARASOL image. Here, the PARASOL image was acquired on 5 May 2006. Thus, Figure 6a could be compared with the true-color PARASOL successive acquisitions shown in Figure 2. Figure 6a shows that the western part of the image (between 2°E and 6°E) is significantly affected by sunglint. The number of sunglint directions depends on the pixel location because each pixel is characterized by its own viewing configuration and wind speed

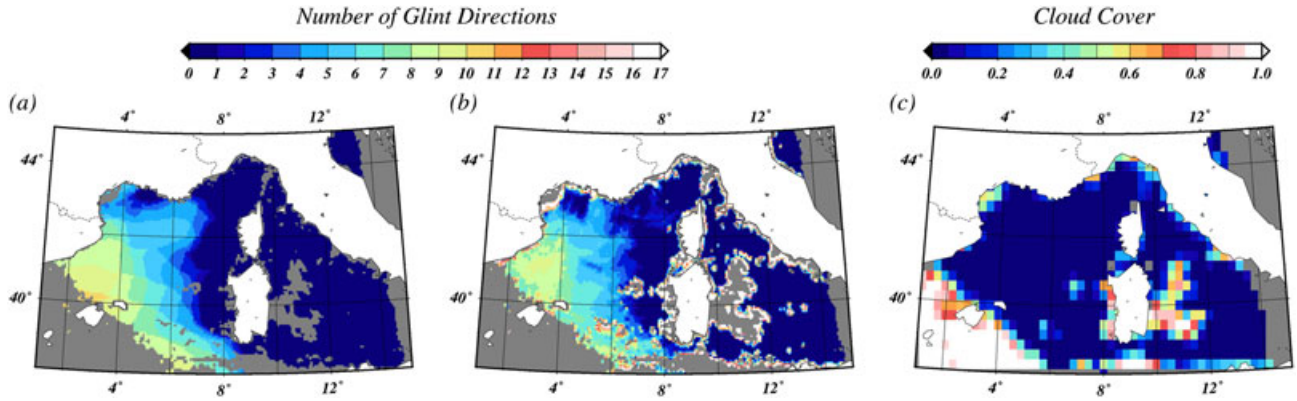

Figure 6. Number of viewing directions affected by sunglint as retrieved from (a) application of the Cox and Munk model using the ECMWF wind speed and wind direction data and (b) application of the "POLAC-glint" algorithm. The pixels over the ocean that were identified as influenced by clouds by the POLAC-glint algorithm are depicted in white in the image. The PARASOL image was acquired on 5 May 2006 over the northwestern Mediterranean Sea. (c) Cloud cover retrieved by the "radiative budget processing line" (CNES) for the corresponding level 2 PARASOL image.

conditions. It should be pointed out that a zone of low sunglint contamination is observed in between a strong sunglint contaminated region near the coastline for the area centered on 43°N and 4°E. This is due to very low wind speed conditions in that area as it has been confirmed by the ECMWF database (wind speeds lower than 2 ms^{-1}). In this area, the roughness of the sea is probably very weak, which is consistent with a decrease of the directional extent of the sunglint.

[28] The application of the POLAC-glint procedure indicates similar patterns (like a high sunglint contamination in the western part of the image) as those observed when using Cox and Munk modeling (Figure 6b). The oceanic pixels that were identified as influenced by clouds are colored in white in the image. The contour of the boundaries of sunglint patterns observed in Figure 6b are finer than those observed for the Cox and Munk model in Figure 6a. The differences observed between the POLAC-glint detection algorithm and Cox and Munk model are mainly ascribed to the fact that wind speed data, which are interpolated from the ECMWF grid in the Cox and Munk standard procedure, have a low spatial resolution in comparison to that of the PARASOL pixels. From this point of view, a low accuracy of the interpolated wind speed data, which are introduced as inputs of the Cox and Munk model, could induce a great uncertainty on the top of atmosphere Stokes parameters.

4.2. Pixels Influenced by Clouds

[29] The identification of cloud-contaminated pixels is crucial because it is a first mandatory step for further retrieval of cloud properties and portion of clear sky conditions. The detection of cloud remains a challenging task, which could lead to errors in the determination of cloud optical or radiative properties and in the subsequent estimation of aerosol properties or ocean color radiometry from space. The potentialities of the application of the POLAC-glint filtering procedures to supplement the already existing cloud detection algorithms are investigated here.

[30] The POLAC atmospheric correction algorithm was applied to level 1 PARASOL data. Note that the PARASOL data were preliminary processed using the cloud mask operational level 1 procedure operated by CNES. The level 1 procedure relies on application of a threshold on the reflectance at the 865 nm band. A more sophisticated cloud mask procedure is operationally applied to obtain the level 2 images dedicated to clouds and radiative budget studies. The level 2 operational procedure relies on series of separated and independent threshold tests applied to each individual pixel and for each viewing direction [*Buriez et al*., 1997; *Parol et al*., 1999]. It should be highlighted that the applications of the algorithms that were developed for cloud detection retrievals for various satellite missions could lead to different results [*Zeng et al*., 2011]. The differences are especially important when dealing with partially cloudy pixels (e.g., broken clouds or cloud edges) or thin clouds like cirrus, as recently underlined by *Zeng et al*. [2011].

[31] Figure 6b shows pixels that are identified as influenced by clouds (depicted in white in the figures) are often located in the vicinity of the clouds identified by the level 1 cloud mask processing chain. A comparison with cloud cover derived from the operational level 2 mask (Figure 6c) shows similar results despite of the reduced spatial resolution of the level 2 data. It is interesting to observe that the POLAC-glint procedure also identified pixels as influenced by clouds that are not detected by the level 2 cloud mask; for example, this fact happens in the region of the image centered on 13°E/40°N (Figures 6b and 6c). These detected cloudy pixels are of small spatial extent. This could explain why those pixels are not identified by the level 2 cloud mask, which makes use of coarser spatial resolution (i.e., 3 by 3 pixels) than the POLAC-glint procedure. For such a coarser spatial resolution, the spatial extent of those clouds spread at the subpixel-scale, which makes their physical signature weaker and their detection even harder with the level 2 product [*Zeng et al*., 2011].

[32] The POLAC-glint filtering procedures almost systematically identify the cloud edges. This is due to two main reasons. First, the huge difference of brightness between white clouds and the dark ocean surface potentially induces a significant atmospheric adjacency effect at satellite level, which can dramatically affect oceanic pixels by wrongly enhancing

the magnitude of their radiance [*Santer and Schmechtig*, 2000]. Second, heterogeneous scenes can result in optically complex pixels with partial cloud cover and/or shadows from nearby clouds. The relatively large ~6 km × 7 km pixel size for PARASOL may result in many such pixels. These types of pixels can reduce the performance of cloud mask processing [*Zeng et al*., 2011], but they can be correctly identified by the POLAC-glint algorithm as cloud edge pixels. Note that, even if this kind of pixels is not directly exploitable for cloud microphysics purposes, it must be identified to exclude erroneous aerosol or ocean color observations when studying time averaged level 3 data. However, it is interesting to notice that more than 13 directions (out of 16 directions of observations) have been identified as sunglint contaminated in the area centered on 6°E/39°N in Figure 6b. A check with other ocean color satellite data (namely SeaWiFS and MERIS sensors) confirmed that this area is not subject to a phytoplankton bloom. Because of the presence of detected cloud edge in the vicinity of those pixels, such a high number of viewing directions identified as sunglint contaminated is likely due to the presence of clouds in this region, which were not correctly handled by the algorithm. Such an example illustrates the main limitation of the POLAC-glint algorithm, which might fail to detect the influence of clouds in regions that are highly impacted by the sunglint contribution (it is worth remembering that the cloud detection is achieved when the Cox and Munk simulation of the sunglint radiance is null).

[33] Figure 7 shows the number of sunglint directions identified by POLAC-glint detection algorithm for PARASOL images acquired on 5 May 2006 over two sites: the western coasts of Africa (Atlantic Ocean) and the island of Madagascar (Indian Ocean). It is observed that the cloud edges (white pixels over oceans in Figure 7) are systematically detected by the POLAC-cloud-edge procedure in the eastern part of the images where sunglint contribution is low or even nonexistent (i.e., number of glint direction is close to zero). However, one could think that a simple expansion or dilatation of the initial operational cloud mask (CNES algorithm) could be applied to identify the cloud edges. Such a dilatation can be simply dependent on the pixel size combined with a typical distance over which a vicinity effect is expected. However, it is interesting to note that the "cloud-pixels" identified by the POLAC algorithm are not systematically located in the direct vicinity of the cloud pixels detected by the operational CNES algorithm. It would be therefore not relevant to perform a simple dilatation of the initial cloud mask. Based on our observation, it would be difficult as well to set an a priori value for the "dilatation parameter" that would be applied. The plus-value of POLAC algorithm is to fully exploit the physical information (multidirectionality, polarization) contained in each individual pixel to carefully detect the cloud edge in contrast to a purely statistic-based approach such as "dilatation" approach, which could lead to meaningless and unrealistic results.

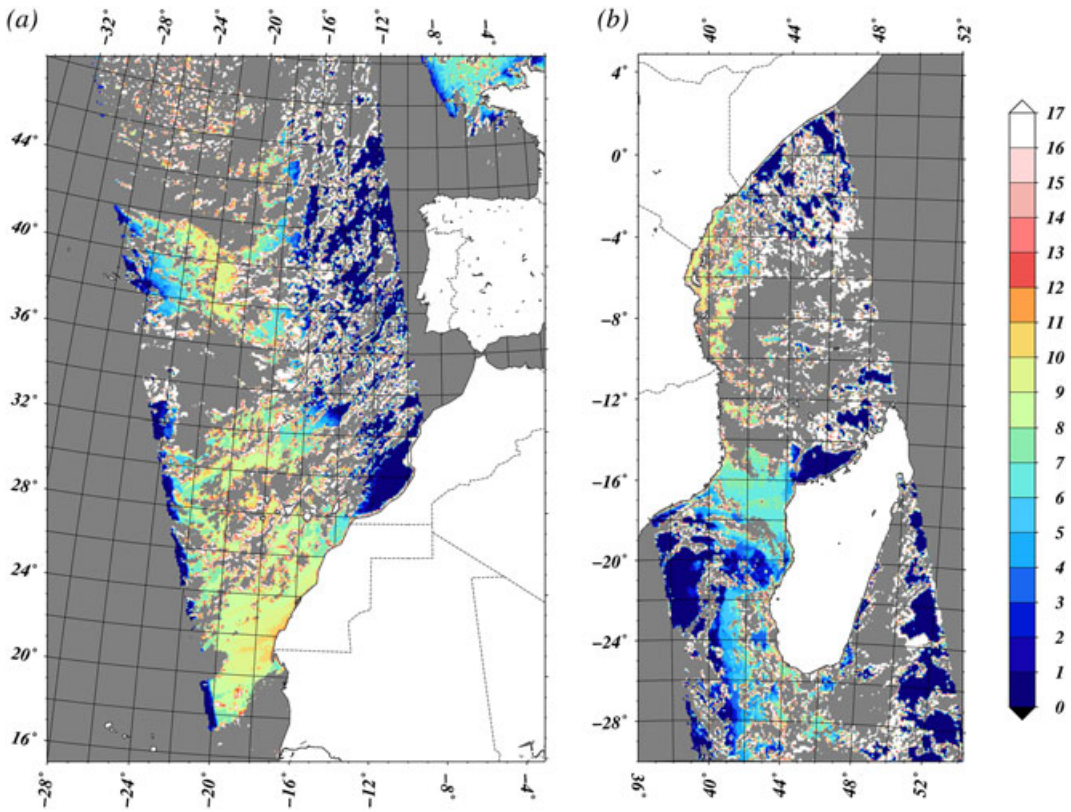

Figure 7. Number of sunglint directions identified by "POLAC-glint" algorithm for PARASOL images acquired on 5 May 2006 offshore (a) the western coasts of Africa and (b) the island of Madagascar. The pixels identified as influenced by clouds by POLAC-glint procedure are colored in white.

[34] In the western part of the images where the contamination by sunglint is the highest, the cloud edges are poorly identified by the POLAC-cloud-edge procedure. This is because the cloud identification procedure relies on the directional dispersion of PARASOL measurements for which the viewing configuration is theoretically away from the sunglint influence. Therefore, for a PARASOL ground target that is located in the western part of the image, the number of sunglint contaminated direction is high while the number of directions away from the glint is too weak to allow efficient cloud-edge detection. Thus, POLAC-cloud-edge detection algorithm could not be strictly applied in highly sunglint contaminated zones. As above mentioned, this is the main limitation of the approach.

[35] The POLAC-cloud-edge algorithm extends the identification of the influence of clouds on pixels. The approach could thus be applied to the worldwide PARASOL data set to quantify pixels that are influenced by clouds. The application of the operational Level 1 PARASOL cloud mask procedure (CNES) to the PARASOL images acquired around the world within a whole day show that about 69% of the pixels over open ocean are identified as totally cloudy (Table 1). The application of the POLAC-cloud-edge procedure shows that about 9% of ocean pixels are detected as influenced by clouds in addition to the 69% of totally cloudy pixels. Therefore, the consideration of these pixels identified using the POLAC-cloud-edge filtering procedure should greatly improve the quality of the aerosol and ocean color products, especially for time-averaged level 3 images. However, it should be highlighted that POLAC-cloud-edge detection method is not able to identify the causes of the partial contamination of a given pixel by clouds (e.g., adjacency effect, broken clouds, cloud edge and shadow, thin cloud). A perspective to overcome this difficulty could be to apply the current existing methods developed for the PARASOL capabilities to the pixels identified by our proposed approach.

Table 1. Percentage of Pixels Identified as Cloudy by the Operational PARASOL Processing (CNES) and Identified as Cloud Edge by the POLAC Filtering Procedures. All the Ocean Pixels of the 14 PARASOL Orbits Covering the Earth on 5 May 2006 are Considered

	Routine Operational PARASOL Processing	POLAC
Procedure	(CNES)	(for all ocean pixels)
Percentage of identified pixels	69.1	9.1

5. Quantification of the Sunglint Radiation and Validation

[36] The ability of the POLAC-glint algorithm to identify directional satellite data contaminated by sunglint regardless of knowledge of sea state has been assessed in the previous sections based on the qualitative analysis of PARASOL image. The quantitative estimation of the sunglint radiation and the validation of the POLAC-glint procedure is now addressed for both the radiance (I) and polarization (Q and U) components of the Stokes vector measured at the top of the atmosphere by the PARASOL sensor. The POLAC-glint algorithm is first applied to all the ocean data acquired by PARASOL around the world to achieve a quantitative evaluation of its performances. Here the images acquired on 5 May 2006 over the world ocean are analyzed.

[37] The sunglint components I_g, Q_g, and U_g retrieved using POLAC-glint method are compared with those calculated using the Cox and Munk model fed with the ECMWF wind speed database (Figure 8). The comparisons show a strong correlation between the two methods, which is in agreement with other studies [*Breon and Henriot*, 2006]. Whatever the Stokes parameter considered (I_g, Q_g, or U_g), the values of the coefficient of determination R^2 are within the range [0.84, 0.92]. In addition, the regression lines are close to the 1:1 line. As illustrated in Figure 8, the slopes of the regression lines vary between 0.88 and 0.96 for the three Stokes parameters. These observed correlations confirm the correctness and the satisfactory performance of POLAC-glint algorithm.

[38] The median of the absolute percentage difference (mAPD, in %), which is defined as 100* $|I_g(\text{POLAC}) - I_g(\text{Cox\&Munk})|/I_g(\text{Cox\&Munk})$ (the same formula is used

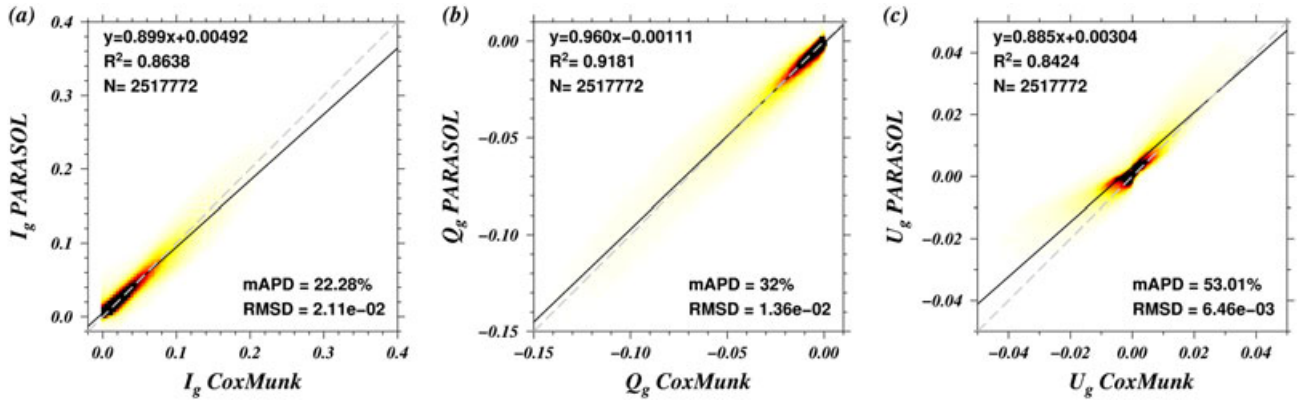

Figure 8. Comparison between the sunglint component of the Stokes parameters (a) I_g, (b) Q_g, and (c) U_g (dimensionless) simulated using Cox and Munk model at the top of the atmosphere at 670 nm (x-axis) and the sunglint Stokes parameters retrieved using POLAC-glint algorithm applied to the PARASOL data acquired over the world on 5 May 2006. N is the number of data considered, mAPD is the median of the absolute percentage difference (in %) and RMSD is the root-mean-square difference.

for the Stokes parameters Q_g and U_g), and the root-mean-square difference (RMSD) are used to evaluate the dispersion of data. The mAPD is about 22% for I_g, 32% for Q_g and increases up to 53% for U_g. However, higher values of mAPD are expected for Q_g and U_g because of the small values of the absolute signal Q_g and U_g, which induce artificially high values of relative differences. Despite of the observed strong correlation, the RMSD remains significantly high with values around 0.021 for each of the Stokes parameters. Let us now compare these RMSD values with the uncertainty of Cox and Munk model outputs (I_g, Q_g, and U_g) when model inputs (e.g., wind speed, wind direction, aerosol optical thickness) vary within their own uncertainties. Numerous comparisons of the ECMWF wind speed data with in situ data acquired using buoys [*Bozzano et al*., 2004; *Ruti et al*., 2008; *Weller and Anderson*, 1996] and with satellite data [*Breon and Henriot*, 2006; *Freilich and Dunbar*, 1999; *Meissner et al*., 2001] were already carried out. Those comparisons revealed discrepancies with a root-mean-square error around $2\,m\,s^{-1}$. Such a value has been used to estimate the statistical uncertainty in sunglint Stokes parameters predicted by the Cox and Munk model using the Gaussian error-propagation principles [e.g., *Kreyszig*, 1970]. It has been observed that at low wind speed values, e.g., $2\,m\,s^{-1}$, the uncertainty in I_g, Q_g, and U_g could be significant even though it is limited to a small range of viewing directions. In addition, at stronger wind speed (e.g., $6\,m\,s^{-1}$), the uncertainty in I_g, Q_g, and U_g spreads into a large range of viewing geometries with values varying often around 0.02 for I_g and Q_g and 0.005 for U_g. Interestingly, these latter values are very consistent to those obtained for the RMSD in Figure 8. This means that the dispersion observed when comparing the estimations of sunglint radiation obtained using POLAC-glint approach and those obtained using Cox and Munk method is in a good agreement with the theoretical expectations of uncertainties in I_g, Q_g, and U_g thus confirming the satisfactory performance of POLAC-glint algorithm.

[39] On the other hand, it should be highlighted that such discrepancies in the normalized radiance measurements may lead to important inaccurate estimates of the aerosol optical thickness, τ_a. For instance, the comparison of the normalized radiances measured for the viewing angle of 5° shown in Figure 4c with the retrieved τ_a obtained in Figure 5 shows that an increase of normalized radiance due to sunglint of 0.02 (which is the difference $\delta I(865)$ observed between the black diamonds and red dots at $\theta_v = 5°$ in Figure 4c) could induce an increase of τ_a of 0.4 (τ_a varies from 0.2 (straight line) to 0.6 (white circle) at $\theta_v = 5°$ in Figure 5). Such a strong sensitivity of the aerosol optical depth to the sunglint signal retrievals demonstrates the advantage and the plus-value of the POLAC-glint algorithm to refine the sunglint Stokes vector estimation.

[40] The sunglint contribution to the top-of-atmosphere signal is mostly driven by specular reflection of the direct Sun light interacting with the ruffled sea surface. The refractive index of the sea water only slightly varies over the visible/near-infrared spectral range. For instance, the refractive index of the pure sea water varies within the range [1.337 to 1.331] between 670 and 865 nm. Theoretical radiative transfer calculations show that the impact of the spectral variation of the refractive index on the terms of the Fresnel matrix is weak (by less than 3%) over the full range of incident angles. Consequently, it is assumed as a first approximation that the specular reflection is spectrally constant over the visible/near infrared spectral range considered in this study. As a result, the sunglint signal at sea level, namely, the term $\mathbf{S_g}$ of equation 2 expressed in unit of normalized radiance (i.e., dimensionless), should theoretically be spectrally flat at sea level. On this basis, the parameters I_g, Q_g, and U_g should not exhibit any spectral variation. Such an optical property of the sunglint pattern can thus be used in a relevant way to validate and check the consistency of the results obtained with the POLAC-glint algorithm when estimating the sunglint contribution of the top-of-atmosphere signal.

[41] Figure 9 shows the histograms of the spectral ratio of Stokes parameters I_g, Q_g, and U_g determined between the wavelengths 865 and 670 nm (for which the marine component of the top of atmosphere signal could be neglected) using the application of POLAC-glint algorithm over the world ocean. The coefficients of the Fresnel reflection matrix

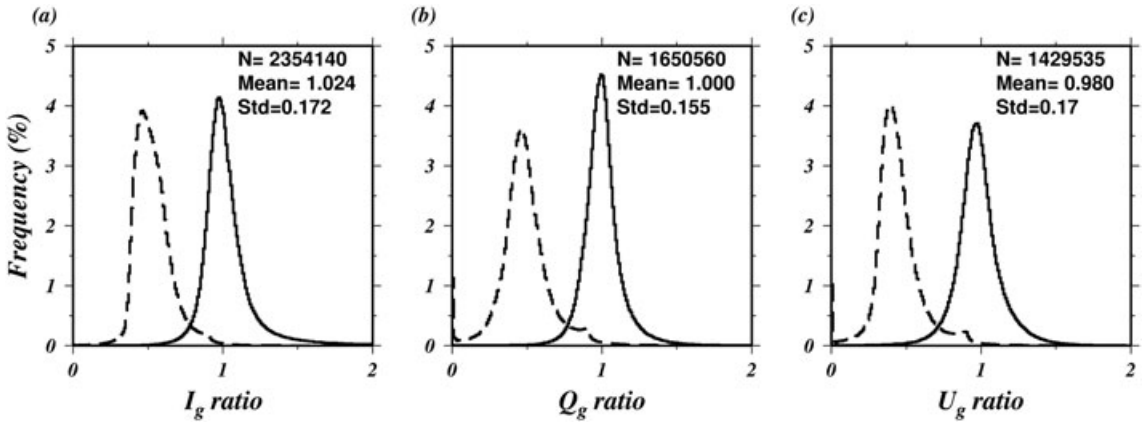

Figure 9. Histograms of the spectral ratio of the Stokes parameters determined between 865 nm and 670 nm (black lines): (a) $I_g(865)/I_g(670)$, (b) $Q_g(865)/Q_g(670)$, and (c) $U_g(865)/U_g(670)$. POLAC-glint algorithm is applied to PARASOL data acquired over the world on 5 May 2006. The dashed line corresponds to the spectral ratio of the Stokes parameters when considering all the pixels over ocean that are located outside of the sunglint pattern as a comparison. *N* is the number of data considered in the processing.

were computed for the given value the refractive index of water at 670 and 865 nm and for each viewing configuration of the PARASOL measurements. The I_g, Q_g, and U_g spectral ratios were then multiplied by the spectral ratios of the respective Fresnel coefficients to remove any residual spectral effect that originates from the spectral variation of therefractive index. Note that the values of the Stokes parameters that are lower than 5 10^{-4} (i.e., PARASOL noise signal) were excluded from the calculation of the spectral ratio to avoid meaningless values. This latter condition explains the fact that the number of data used to plot the histograms of I_g, Q_g, or U_g (i.e., values of N in Figures 9a–9c) differ between each figure.

[42] The histograms reveal that the distributions of the spectral ratio of the sunglint Stokes parameters are centered on the value of 1, which is consistent with a spectrally flat variation. More precisely, an average spectral variation less than 2% is observed for the three Stokes parameters I_g, Q_g, and U_g. Such results clearly demonstrate the consistency of the derived spectral shapes of sunglint Stokes parameters with the theoretical expectations. The dispersion observed in the histograms around the mean value can originate from many instrumental or geophysical error sources such as the presence of whitecaps or absorbing component of aerosols (which is not accounted for in the current version of the POLAC algorithm). Such a dispersion could be used here as an evaluation of our product accuracy. Figure 9 reports the mean and standard deviation values of the histograms. Based on our results, the relative accuracy of our method is less than 17.3% (this value is obtained by dividing the standard deviation value to the mean) for all the Stokes parameters.

[43] To emphasize the fact that the sole sunglint pattern is supposed to exhibit a spectral flat behavior in the PARASOL data, the histograms of the spectral ratio of the Stokes parameters measured for pixels that are not contaminated by sunglint (i.e., pixels that are located out of the sunglint influence) are also shown in Figure 9 (dashed lines). The distributions of these latter histograms are centered on the value of 0.5 for the three Stokes parameters. Such a value of 0.5, which is far from unity, reveals the occurrence of a significant spectral variation of the Stokes parameters when the ground target is not influenced by sunglint. The existence of a spectral variation is simply due to the optical properties of the atmospheric layer and ground target when this target is not subject to sunglint influence.

6. Conclusion

[44] In this paper, the contributions of the sunglint signal to the TOA radiance (Stokes parameter I) and polarization state of light (Stokes parameters Q and U) were estimated using an original algorithm (so-called POLAC-glint) that exploits the multidirectional and polarized properties of radiation. This topic is of great interest to correct satellite data for sunlight contamination prior to applying any inversion algorithms dedicated to retrieve aerosol properties and ocean color radiometry. Estimation of sunglint radiation to the TOA signal is also useful for many other remote sensing applications such as sensor calibration, sea state monitoring or estimation of absorbing aerosols.

[45] In the first part of the paper, the POLAC-glint algorithm was described. The sunglint detection procedure used within POLAC-glint fully exploits the multidirectional properties of a satellite ground target. The main principles of the approach could be summarized as follows. A given ground target is observed for several viewing directions. The aerosol optical depth is supposed to weakly vary along all the directions of observation of this ground target. If a viewing direction is influenced by sunglint, the aerosol optical depth will be highly overestimated. Comparisons between the aerosol optical depth values derived for the various geometries of observation of a given ground target allows identifying directions that are contaminated by the sunglint. Based on this detection, the algorithm consists in first determining the aerosol optical properties and water-leaving radiance from directional measurements outside of the glint. Then, those retrievals are used to derive the Stokes vector (radiance plus polarization) of the directional sunglint signal.

[46] The major originality of the POLAC-glint algorithm is that it does not require any assumptions on the actual sea state as it is commonly made in previous studies. The POLAC-glint algorithm was successfully adjusted based on a priori knowledge in the wind speed values to detect cloud edge pixels over the ocean. Note that the uncertainty value in wind speed of 1 m s^{-1}, which is consistent with the typical accuracy of wind speed data that are commonly used for remote sensing applications, was considered. The method was termed "POLAC-cloud-edge" in the paper. POLAC-cloud-edge algorithm allows to extend the mask cloud procedure, which is currently used within the operational PARASOL data processing. The data analyzed here over the world ocean using POLAC-cloud-edge method showed that a supplementary ratio of 9% of ocean pixels that were not detected by the standard operational cloud mask procedure should be removed due to a partial contamination by cloud (i.e., cloud edge). The example that is provided in the paper for a given day of PARASOL acquisitions over the entire globe reveals that the use of POLAC-cloud-edge algorithm together with the use of the standard operational PARASOL cloud mask procedure detected 78% of pixels that are totally and partially contaminated by cloud influence. As a comparison, the use of the sole standard PARASOL cloud mask detected only 69% of pixels contaminated by clouds over the entire globe for the same PARASOL acquisitions.

[47] The validation of POLAC-glint algorithm was performed in two steps. First, comparisons of the sunglint component of the I_g, Q_g, and U_g Stokes parameters retrieved with POLAC-glint using PARASOL acquisitions obtained over the entire globe were carried out with those estimated using Cox and Munk model and ECMWF wind speed database. Result shows that a strong correlation ($R^2 > 0.84$) was obtained between both methods with dispersion (i.e., RMSD) lower than 0.02 for each Stokes parameter. Second, the spectral property of the sunglint signal, which theoretically exhibits a spectrally flat variation, was used to evaluate the performance of POLAC-glint algorithm. A data set acquired by PARASOL sensor over the world ocean for the entire globe was analyzed. The data set covers various aerosols and sea surface conditions. Results showed that the spectral ratio of the three Stokes parameters derived between 865 and 670 nm is virtually neutral (i.e., close to 1).

More precisely, the average values of the spectral ratio of the Stokes parameters between both wavelengths were 1.02, 1.00, and 0.98 for I, Q, and U, respectively. The analysis demonstrates the capacity of POLAC-glint algorithm to achieve accurate estimation of the sunglint radiation by exploiting directional and polarization information exclusively contained within the PARASOL measurements. Note that it is the first time, to our knowledge, that the polarized components of the sunglint pattern (Q and U Stokes parameters) and their spectral properties are used in a relevant way to (i) improve the detection of sunglint and (ii) to validate the consistency of the obtained results.

[48] Typical perspectives of this work could consist of using the estimation of the sunglint radiation as derived by POLAC-glint algorithm: (i) to determine the wind speed value for each pixel of the satellite images; such a wind speed value could thus be further used to estimate the white-cap contribution, (ii) to reappraise sea state retrieval and the subsequent wave slopes distribution, (iii) to ensure more reliable sunglint data for satellite calibration purposes and (iv) to refine the retrieval of geophysical parameter based on sunglint observation (e.g., water vapor content, absorbing aerosols). The results obtained in this study are potentially applicable to any multidirectional satellite missions such as the forthcoming satellite mission "Preparatory Aerosols, Clouds and Ecosystems (PACE)" (NASA, USA) or the "Multidirectional, Multipolarization and Multispectral (3MI)" mission (European Space Agency and EUMETSAT organization) which are both scheduled for launch around 2018.

[49] **Acknowledgments.** The authors would like to thank Centre National d'Etudes Spatiales (CNES) and ACRI-ST Company for funding the doctoral fellowship of Tristan Harmel. This research was supported by French program Programme National de Télédétection Spatiale (PNTS) of the Institut National des Sciences de l'Univers (INSU) through the project ALGOPOL. The authors would like to thank the organization ICARE (Laboratoire d'Optique Atmosphérique and CNES) for providing the PARASOL geophysical products. We are grateful to J. L. Deuzé and P. Goloub for providing aerosol models that were used in POLAC algorithm. The authors would also like to thank the reviewers for their relevant comments and suggestions, which enhance the quality of the paper.

References

Antoine, D., and A. Morel (1999), A multiple scattering algorithm for atmospheric correction of remotely sensed ocean colour (MERIS instrument): principle and implementation for atmospheres carrying various aerosols including absorbing ones, *Int. J. remote Sens.*, *20*, 1875–1916, <Go to ISI>://000081047400014.

Aoki, T., T. Aoki, and M. Fukabori (2002), Path-radiance correction by polarization observation of Sun glint glitter for remote measurements of tropospheric greenhouse gases, *Appl. Opt.*, *41*, 4945–4957.

Bozzano, R., A. Siccardi, M. E. Schiano, M. Borghini, and S. Castellari (2004), Comparison of ECMWF surface meteorology and buoy observations in the Ligurian Sea, *Annales Geophysicae*, *22*, 317–330.

Breon, F. M., and N. Henriot (2006), Spaceborne observations of ocean glint reflectance and modeling of wave slope distributions, *J. Geophys. Res.-Oceans*, *111*, C06005.

Breon, F. M., A. Vermeulen, and J. Descloitres (2011), An evaluation of satellite aerosol products against sunphotometer measurements, *Remote Sens. Environ.*, *115*, 3102–3111.

Buriez, J. C., C. Vanbauce, F. Parol, P. Goloub, M. Herman, B. Bonnel, Y. Fouquart, P. Couvert, and G. Seze (1997), Cloud detection and derivation of cloud properties from POLDER, *Int. J. remote Sens.*, *18*, 2785–2813.

Chami, M. (2007), Importance of the polarization in the retrieval of oceanic constituents from the remote sensing reflectance, *J. Geophys. Res.-Oceans*, *112*, C05026, <Go to ISI>://000246839800007.

Chami, M., R. Santer, and E. Dilligeard (2001), Radiative transfer model for the computation of radiance and polarization in an ocean-atmosphere system: polarization properties of suspended matter for remote sensing, *Appl. Opt.*, *40*, 2398–2416.

Chowdhary, J., B. Cairns, F. Waquet, K. Knobelspiesse, M. Ottaviani, J. Redemann, L. Travis, and M. Mishchenko (2012), Sensitivity of multiangle, multispectral polarimetric remote sensing over open oceans to water-leaving radiance: Analyses of RSP data acquired during the MILAGRO campaign, *Remote Sens. Environ.*, *118*, 284–308, http://www.sciencedirect.com/science/article/pii/S0034425711003981

Chust, G., and Y. Sagarminaga (2007), The multi-angle view of MISR detects oil slicks under sun glitter conditions, *Remote Sens. Environ.*, *107*, 232–239.

Coulson, K. L. (1988), *Polarization and Intensity of Light in the Atmosphere*, A. Deepak Pub., Hampton, Va., USA.

Cox, C., and W. Munk (1954a), Measurement Of The Roughness Of The Sea Surface From Photographs Of The Suns Glitter, *J. Opt. Soc. Am.*, *44*, 838–850.

Cox, C., and W. Munk (1954b), Statistics Of The Sea Surface Derived From Sun Glitter, *Journal Of Marine Research*, *13*, 198–227.

Cox, C., and W. Munk (1956), Slopes of the sea surface deduced from photographs of sun glitter, Scripps Institution of Oceanography.

Darecki, M., D. Stramski, and M. Sokolski (2011), Measurements of high-frequency light fluctuations induced by sea surface waves with an Underwater Porcupine Radiometer System, *J. Geophys. Res*, *116*, C00H09.

Deschamps, P. Y., F. M. Breon, M. Leroy, A. Podaire, A. Bricaud, J. C. Buriez, and G. Seze (1994), The Polder Mission - Instrument Characteristics And Scientific Objectives, *IEEE T. Geosci. Remote*, *32*, 598–615.

Deuze, J. L., F. M. Breon, C. Devaux, P. Goloub, M. Herman, B. Lafrance, F. Maignan, A. Marchand, F. Nadal, G. Perry, and D. Tanre (2001), Remote sensing of aerosols over land surfaces from POLDER-ADEOS-1 polarized measurements, *J. Geophys. Res.-Atmos.*, *106*, 4913–4926, <Go to ISI>://000167482900017.

Deuze, J. L., P. Goloub, M. Herman, A. Marchand, G. Perry, S. Susana, and D. Tanre (2000), Estimate of the aerosol properties over the ocean with POLDER, *J. Geophys. Res.-Atmos.*, *105*, 15329–15346, <Go to ISI>://000087844900015.

Dickey, T. D., G. W. Kattawar, and K. J. Voss (2011), Shedding new light on light in the ocean, *Physics Today*, *64*, 44–49.

Ebuchi, N., and S. Kizu (2002), Probability distribution of surface wave slope derived using sun glitter images from Geostationary Meteorological Satellite and surface vector winds from scatterometers, *J. Oceanogr.*, *58*, 477–486.

Fougnie, B., G. Bracco, B. Lafrance, C. Ruffel, O. Hagolle, and C. Tinell (2007), PARASOL in-flight calibration and performance, *Appl. Opt.*, *46*, 5435–5451, <Go to ISI>://000249167100074.

Freilich, M. H., and R. S. Dunbar (1999), The accuracy of the NSCAT 1 vector winds: Comparisons with National Data Buoy Center buoys, *J. Geophys. Res.*, *104*, 11231–11246.

Frouin, R., M. Schwindling, and P.-Y. Deschamps (1996), Spectral reflectance of sea foam in the visible and near-infrared: In situ measurements and remote sensing implications, *J. Geophys. Res.*, *101*, 14361–14371, http://dx.doi.org/10.1029/96JC00629.

Fukushima, H., A. Higurashi, Y. Mitomi, T. Nakajima, T. Noguchi, T. Tanaka, and M. Toratani (1998), Correction of atmospheric effects on ADEOS/OCTS ocean color data: algorithm description and evaluation of its performance, *J. Oceanogr.*, *54*, 417–430.

Gao, B. C., and Y. J. Kaufman (2003), Water vapor retrievals using Moderate Resolution Imaging Spectroradiometer (MODIS) near-infrared channels, *J. Geophys. Res*, *108*, 4389.

Gordon, H. R. (1978), Removal of atmospheric effects from satellite imagery of the oceans, *Appl. Opt.*, *17*, 1631–1636.

Gordon, H. R. (1997), Atmospheric correction of ocean color imagery in the Earth Observing System era, *J. Geophys. Res.*, *102*, 17081–17106.

Gordon, H. R., and O. B. Brown (1974), Influence of Bottom Depth and Albedo on the Diffuse Reflectance of a Flat Homogeneous Ocean, *Appl. Opt.*, *13*, 2153–2159, http://ao.osa.org/abstract.cfm?URI=ao-13-9-2153

Gordon, H. R., and D. K. Clark (1981), Clear water radiances for atmospheric correction of coastal zone color scanner imagery, *Appl. Opt.*, *20*, 4175–4180.

Gordon, H. R., and M. Wang (1994), Retrieval of water leaving radiance and aerosol optical thickness over the oceans with seawifs: a preliminary algorithm, *Appl. Opt.*, *33*, 443–458.

Hagolle, O., J. M. Nicolas, B. Fougnie, F. Cabot, and P. Henry (2004), Absolute calibration of VEGETATION derived from an interband method based on the sun glint over ocean, *IEEE T. Geosci. Remote*, *42*, 1472–1481, <Go to ISI>://000222723400014.

Harmel, T., and M. Chami (2008), Invariance of polarized reflectance measured at the top of atmosphere by PARASOL satellite instrument in the visible range with marine constituents in open ocean waters, *Opt. Express*, *16*, 6064–6080, http://dx.doi.org/10.1364/OE.16.006064.

Harmel, T., and M. Chami (2011), Influence of polarimetric satellite data measured in the visible region on aerosol detection and on the performance of atmospheric correction procedure over open ocean waters, *Opt. Express*, *19*, 20960–20983.

Harmel, T., and M. Chami (2012), Determination of sea surface wind speed using the polarimetric and multidirectional properties of satellite measurements in visible bands, *Geophys. Res. Lett.*, *39*, L19611, doi: 10.1029/2012GL053508.

Herman, M., J. L. Deuze, A. Marchand, B. Roger, and P. Lallart (2005), Aerosol remote sensing from POLDER/ADEOS over the ocean: Improved retrieval using a nonspherical particle model, *J. Geophys. Res.-Atmos.*, *110*, 1–11, <Go to ISI>://000227641900002.

Hu, C. (2010), An empirical approach to derive MODIS ocean color patterns under severe sun glint, *Geophys. Res. Lett.*, *38*, L01603.

Hu, C., X. Li, W. G. Pichel, and F. E. Muller-Karger (2009), Detection of natural oil slicks in the NW Gulf of Mexico using MODIS imagery, *Geophys. Res. Lett*, *36*, L01604.

Hulburt, E. O. (1934), Polarization of light at sea, *J. Opt. Soc. Am.*, *24*, 35–42.

Jackson, C. (2007), Internal wave detection using the moderate resolution imaging spectroradiometer (MODIS), *J. Geophys. Res*, *112*, C11012, doi:10.1029/2007JC004220.

Kattawar, G. W., G. N. Plass, and S. J. Hitzfelder (1976), Multiple scattered radiation emerging from Rayleigh and continental haze layers. 1: Radiance, polarization, and neutral points, *Appl. Opt.*, *15*, 632–647, http://dx.doi.org/10.1364/AO.15.000632.

Kaufman, Y. J., J. V. Martins, L. Remer, M. R. Schoeberl, and M. A. Yamasoe (2002), Satellite retrieval of aerosol absorption over the oceans using sunglint, *Geophys. Res. Lett.*, *29*, 34–31.

Kay, S., J. D. Hedley, and S. Lavender (2009), Sun Glint Correction of High and Low Spatial Resolution Images of Aquatic Scenes: a Review of Methods for Visible and Near-Infrared Wavelengths, *Remote Sensing*, *1*, 697–730.

Kleidman, R. G., Y. J. Kaufman, B. Gao, Cai, L. A. R., V. G. Brackett, R. A. Ferrare, E. V. Browell, and S. Ismail (2000), Remote sensing of total precipitable water vapor in the near‐IR over ocean glint, *Geophys. Res. Lett.*, *27*, 2657–2660, http://dx.doi.org/10.1029/1999GL011156.

Koepke, P. (1984), Effective Reflectance Of Oceanic Whitecaps, *Appl. Opt.*, *23*, 1816–1824.

Kokhanovsky, A. A. (2004a), Single light scattering: Bubbles versus droplets, *American Journal of Physics*, *72*, 258, doi:10.1119/1.1621030.

Kokhanovsky, A. A. (2004b), Spectral reflectance of whitecaps, *J. Geophys. Res*, *109*, C05021, doi:10.1029/2003JC002177.

Kotchenova, S. Y., E. F. Vermote, R. Matarrese, and F. J. Klemm (2006), Validation of a vector version of the 6S radiative transfer code for atmospheric correction of satellite data. Part I: Path radiance, *Appl. Opt.*, *45*, 6762–6774, <Go to ISI>://000240355100017.

Kreyszig, E. (1970), *Introductory mathematical statistics: principles and methods*, Wiley, New York.

Meissner, T., D. Smith, and F. Wentz (2001), A 10 year intercomparison between collocated Special Sensor Microwave Imager oceanic surface wind speed retrievals and global analyses, *J. Geophys. Res*, *106*, 731–711.

Mishchenko, M. I., I. V. Geogdzhayev, B. Cairns, B. E. Carlson, J. Chowdhary, A. A. Lacis, L. Liu, W. B. Rossow, and L. D. Travis (2007), Past, present, and future of global aerosol climatologies derived from satellite observations: A perspective, *J. Quant. Spectrosc. Radiat. Transfer*, *106*, 325–347, <Go to ISI>://000247510300028.

Monahan, E. C. (1971), Oceanic whitecaps, *J. Phys. Oceanogr.*, *1*, 139–144.

Nicolas, J. M., P. Y. Deschamps, and O. Hagolle (2006), Radiometric calibration of the visible and near-infrared bands of SEVIRI using rayleigh scattering and Sun-glint over oceans, *Proceedings Of The 3rd Msg Rao Workshop*, *619*, 19–24, <Go to ISI>://000241724100004.

Ottaviani, M., R. Spurr, K. Stamnes, W. Li, W. Su, and W. Wiscombe (2008a), Improving the description of sunglint for accurate prediction of remotely sensed radiances, *J. Quant. Spectrosc. Radiat. Transfer*, *109*, 2364–2375.

Ottaviani, M., K. Stamnes, J. Koskulics, H. Eide, S. R. Long, W. Su, and W. Wiscombe (2008b), Light Reflection from Water Waves: Suitable Setup for a Polarimetric Investigation under Controlled Laboratory Conditions, *J. Atmos. Ocean. Technol.*, *25*, 715–728.

Parol, F., J. C. Buriez, C. Vanbauce, P. Couvert, G. Seze, P. Goloub, and S. Cheinet (1999), First results of the POLDER "Earth Radiation Budget and Clouds" operational algorithm, *IEEE T. Geosci. Remote*, *37*, 1597–1612.

Parol, F., J. C. Buriez, C. Vanbauce, J. Riedi,L. C. Labonnote, M. Doutriaux-Boucher, M. Vesperini, G. Sèze, P. Couvert, and M. Viollier (2004), Review of capabilities of multi-angle and polarization cloud measurements from POLDER, *Advances in Space Research*, *33*, 1080–1088.

Remer, L. A., Y. J. Kaufman, D. Tanré, S. Mattoo, D. A. Chu, J. V. Martins, R. R. Li, C. Ichoku, R. C. Levy, R. G. Kleidman, T. F. Eck, E. Vermote, and B. N. Holben (2005), The MODIS Aerosol Algorithm, Products, and Validation, *J. Atmos. Sci.*, *62*, 947–973, http://dx.doi.org/10.1175%2FJAS3385.1.

Ross, V., and D. Dion (2007), Sea surface slope statistics derived from Sun glint radiance measurements and their apparent dependence on sensor elevation, *J. Geophys. Res.*, *112*, C09015.

Ruti, P. M., S. Marullo, F. D'Ortenzio, and M. Tremant (2008), Comparison of analyzed and measured wind speeds in the perspective of oceanic simulations over the Mediterranean basin: Analyses, QuikSCAT and buoy data, *Journal of Marine Systems*, *70*, 33–48.

Santer, R., and C. Schmechtig (2000), Adjacency effects on water surfaces: primary scattering approximation and sensitivity study, *Appl. Opt.*, *39*, 361–375.

Steinmetz, F., P. Y. Deschamps, and D. Ramon (2011), Atmospheric correction in presence of sun glint: application to MERIS, *Opt. Express*, *19*, 9783–9800.

Tanre, D., M. Herman, P. Y. Deschamps, and A. Deleffe (1979), Atmospheric Modeling For Space Measurements Of Ground Reflectances, Including Bidirectional Properties, *Appl. Opt.*, *18*, 3587–3594.

Tanre, D., Y. J. Kaufman, M. Herman, and S. Mattoo (1997), Remote sensing of aerosol properties over oceans using the MODIS/EOS spectral radiances, *J. Geophys. Res.-Atmos.*, *102*, 16971–16988, <Go to ISI>://A1997XN38400042.

Torrance, K. E., E. M. Sparrow, and R. C. Birkebak (1966), Polarization, directional distribution, and off-specular peak phenomena in light reflected from roughened surfaces, *JOSA*, *56*, 916–924.

Toubbe, B., T. Bailleul, J. L. Deuze, P. Goloub, O. Hagolle, and M. Herman (1999), In-flight calibration of the POLDER polarized channels using the sun's glitter, *IEEE T. Geosci. Remote*, *37*, 513–525, <Go to ISI>://000078122700017.

Vermote, E. F., D. Tanre, J. L. Deuze, M. Herman, and J. J. Morcrette (1997), Second Simulation of the Satellite Signal in the Solar Spectrum, 6S: An overview, *IEEE T. Geosci. Remote*, *35*, 675–686, <Go to ISI>://A1997WZ43300018.

Wang, M., and S. W. Bailey (2001), Correction of sun glint contamination on the SeaWiFS ocean and atmosphere products, *Appl. Opt.*, *40*, 4790–4798.

Weller, R. A., and S. P. Anderson (1996), Surface meteorology and air-sea fluxes in the western equatorial Pacific warm pool during the TOGA Coupled Ocean-Atmosphere Response Experiment, *J. Clim.*, *9*, 1959–1990.

You, Y., G. W. Kattawar, K. J. Voss, P. Bhandari, J. Wei, M. Lewis, C. J. Zappa, and H. Schultz (2011), Polarized light field under dynamic ocean surfaces: Numerical modeling compared with measurements, *J. Geophys. Res.*, *116*, C00H05.

Zeng, S., F. Parol, J. Riedi, C. Cornet, and F. Thieuleux (2011), Examination of POLDER/PARASOL and MODIS/Aqua Cloud Fractions and Properties Representativeness, *Bull. Am. met. Soc.*, *24*, 4435–4450.

Zhang, H., and M. Wang (2010), Evaluation of sun glint models using MODIS measurements, *J. Quant. Spectrosc. Radiat. Transfer*, *111*, 492–506, doi: 10.1016/j.jqsrt.2009.10.001.